Special interphase orientation relationships and locked lamellar growth in thin In-In2Bi eutectics

Sabine Bottin-Rousseau, Oriane Senninger, Gabriel Faivre, Silvère Akamatsu

Special interphase orientation relationships and locked lamellar growth patterns in thin In-In_2Bi eutectics

Sabine Bottin-Rousseau,[1] Oriane Senninger,[1,2] Gabriel Faivre,[1] and Silvère Akamatsu[1]

[1] *Sorbonne Universités, UPMC Univ Paris 6, CNRS-UMR 7588, Institut des NanoSciences de Paris, case courrier 840, 4 place Jussieu, 75252 Paris Cedex 05, France*

[2] *CEMEF, France*

(Dated: November 28, 2017)

Lamellar eutectic alloys have two main modes of growth (floating or locked) depending on the orientation of the two eutectic phases. According to recent theoretical studies [Ghosh *et al*, Phys. Rev. E **91**, 022407 (2015)], the key factor is the existence or otherwise of a sufficiently deep minimum in the surface energy plot of the interphase boundaries. We present an experimental study aiming at testing this prediction. We used a near-eutectic In-In_2Bi alloy that solidifies into a tetragonal phase ϵ (In-11.5 at%Bi) and a hexagonal phase δ (In_2Bi). Thin samples of this alloy were solidified using a rotating directional solidification stage and analyzed for crystallographic texture by X-ray diffraction. A series of samples with low (1 to 3°) mosaic spreads were found to contain either of the following coincidence relationships: $A = \{2\bar{1}\bar{1}0\}^{\delta} /\!/ \{111\}^{\epsilon}$ or $E = \{1\bar{1}02\}^{\delta} /\!/ \{111\}^{\epsilon}$. The *A*-type samples exhibited a locked mode of growth, and the *E*-type samples a floating mode of growth. Given that, according to standard crystallographic criteria, *A*-type interphase boundaries have a much smaller surface energy than *E*-type ones, these findings are in agreement with the theoretical predictions.

PACS numbers: ?????

I. INTRODUCTION

Directionally solidified lamellar eutectic alloys often grow with special interphase orientation relationships, the term special meaning that a coincidence relationship between some low-index lattice planes of the two eutectic phases is achieved [1–5]. The consequences of this fact on the growth dynamics of lamellar eutectics are rarely mentioned. Yet, an interphase boundary lying parallel to two coincident low-index lattice planes must have a particularly low energy [6]. Consequently, the surface-energy plot of the interphase boundary (γ_B-plot) in a eutectic grain (EG) – *i.e.* a region of uniform orientation of the two eutectic phases – with a special interphase orientation relationship must have a deep minimum in the direction of the coincident lattice planes and, more globally, be strongly anisotropic.

There has been much recent progress on the issue of the growth dynamics of lamellar eutectics with strongly anisotropic γ_B-plots, at least in thin samples. It was shown experimentally that thin eutectic grains should be classified into three main categories according to the nature (floating, locked or nearly locked) of the growth dynamics they display [8]. A floating EG is recognizable by two main features: eutectic lamellae grow parallel to the thermal gradient; the interlamellar spacing undergoes a continuous process of homogenization called spacing-diffusion [7]. Conversely, in a locked EG, eutectic lamellae run parallel to some fixed crystallographic direction even if it is tilted to a large angle from the thermal gradient axis, and the interlamellar spacing distribution does not change appreciably over time even if it is strongly non-uniform [8]. The intermediate nearly locked category comprises all the EGs, in which eutectic lamellae are tilted to a noticeable angle with respect to the thermal gradient but nevertheless undergo an efficient spacing-diffusion process. Theoretical and numerical studies showed that these different dynamics are related to different degrees of anisotropy of the interphase boundary – the anisotropy of the solid-liquid interfaces being assumed to be negligible in lamellar eutectics [9, 10]. In brief, according to these studies, floating EGs have nearly isotropic γ_B-plots, locked EGs have γ_B-plots with deep minima in directions that corresponds to locked lamellar planes, and nearly locked EGs have γ_B-plots with relatively shallow minima that attract, but do not lock, the lamellar planes. Floating and nearly locked EGs will be jointly referred to as "floating" henceforth.

These theoretical views are self-consistent but have not yet been tested by means of a simultaneous study of interphase orientation relationships and lamellar growth dynamics. In this article, we present a real-time observation study of lamellar patterns in thin-sample directional solidification of a near-eutectic In-In_2Bi alloy coupled with crystal orientation measurements by X-ray diffraction. The In-In_2Bi alloy is used here as a convenient and well-characterized low-melting point model eutectic alloy [7]. The use of a rotating directional solidification stage allows a grain-by-grain study of the γ_B-plot. The results demonstrate a strong correlation between special interphase orientation relationships and anisotropy effects on lamellar eutectic growth, in agreement with the theoretical predictions. They also provide information about the preferred interphase orientation relationships of the In-In_2Bi alloy and their mechanism of formation.

II. METHODS

A. Alloy and samples

Details about the alloy and the experimental methods used during this study can be found elsewhere [7, 8]. We will limit ourselves to a few points. The In-Bi phase diagram has a eutectic point at 72.7° and 22.5 at%Bi [11]. The eutectic solid phases are a tetragonal solid solution ϵ (In-11.5 at%Bi) and the hexagonal intermetallic compound δ (In_2Bi). The ϵ phase decomposes eutectoidally into δ and a tetragonal terminal solid solution (In-8at%Bi) at about 49°.

The ϵ and (In) phases have most often been described as body centered tetragonal with two atoms per unit cell, but may also be described as face centered tetragonal (fct) with four atoms per unit cell [12, 13]. The latter option, which allows ϵ and (In) to be viewed as slightly deformed face centered cubic crystals, is adopted here. The δ phase has a hexagonal Ni_2In structure with six atoms per unit cell. The Miller notation of its lattice directions is adopted here. Table I gives the lattice parameters of the different phases as measured from our eutectic alloy by X-ray powder diffraction.

Phase	a [Å]	c [Å]	c/a
δ	5.496	6.585	1.198
ϵ	4.914	4.490	0.914
(In)	4.600	5.019	1.091

TABLE I. Lattice parameters of the eutectic and eutectoid phases (this study). A fct unit cell is used for ϵ and (In).

A slightly hypereutectic In-In_2Bi alloy was used. This alloy forms regular ϵ-δ lamellar patterns with a volume phase fraction of about 0.5 during directional solidification. Figure 1a describes the directional-solidification samples and coordinate system used here. The alloy is enclosed between two 0.3 mm-thick glass plates separated by a 13 μm-thick funnel-shaped spacer delimiting a 0.1 mm-wide grain selector at one end of the sample and a 30 mm-wide space outside the selector. The molten alloy is introduced into this container by a vacuum suction method and then solidified by rapid cooling to room temperature (primary solidification). The sample is then inserted into the directional solidification setup and placed under a undirectional thermal gradient (0.9 Kmm^{-1}) in such a position that the 72.7°C isotherm, and thus the solid-liquid interface, are located inside the selector. The part of the sample that remains solid serves as seed for the forthcoming solidification process. During this process, the growth front and the solid behind it are observed through the upper glass lid of the sample using reflected-light microscopy. A scanning of the growth front over the whole sample width is performed at regular intervals. Images are recorded with a monochrome digital camera, and transferred to a computer for further analysis.

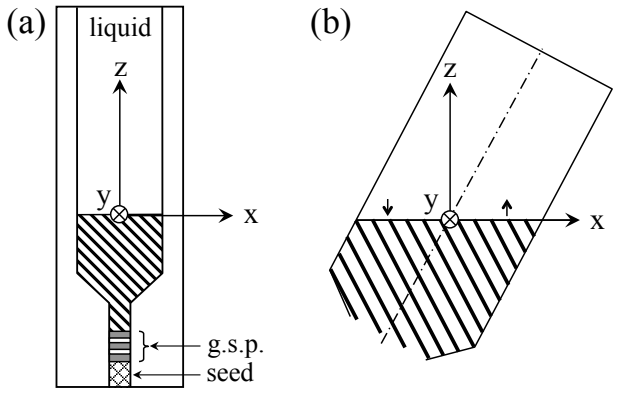

FIG. 1. Solidification processes. The thermal gradient is directed along the **z** axis. The sample plane lies parallel to the **xz** plane. (a) Standard directional solidification. The sample is being pulled in the **-z** direction. g.s.p.: grain selection process. (b) Rotating directional solidification. The sample is being rotated anticlockwise about the **y** axis. Arrows: directions of motion with respect to the liquid.

B. Grain selection process

The first and critical stage of a solidification run consists of growing a single eutectic grain that exhibits a well-characterized (floating or locked) eutectic growth dynamics. A description of the method used for this purpose can be found elsewhere [7, 8, 14]. We limit ourselves to the following points. The grain selection process is conducted in such a way that one EG overgrows the seed and fills the whole sample width. The monocrystallinity of the emerging EG as well as the nature of its growth dynamics can be qualitatively assessed in real time, allowing one to decide immediately on the continuation or reset of the solidification run. A quantitative assessment of crystal quality performed by XRD diffraction at the end of the solidification run leads to the eventual recruitment or rejection of the sample. Five locked samples (1 to 5) and four floating ones (6 to 9) were used during this study. Unexpectedly, some samples (1 to 3) contained two interrelated EGs instead of one, with interesting consequences. We will return to this point later on. The nine selected samples turned out to contain only two types of special EGs, as will be seen below. This does not mean that no other types of EGs were present in the seed, but only that, if there were, they were eliminated during the grain selection process.

C. Rotating directional solidification

The solidification setup used during this study allows one to switch between standard directional solidifica-

tion (DS) and rotating directional solidification (RDS) – *i.e.* between translation and rotation with respect to the thermal gradient (Fig. 1). RDS-runs are usually pursued over several complete revolutions of the sample. Although the grown microstructure is destroyed by melting after a half turn, an uninterrupted recording of the growth front allows one to perform retroactively a reconstruction, or space-time map, of the whole solidification process. It has been shown that the trajectories of the interphase boundaries generated during RDS are approximately homothetic to the 2D Wulff form of the interphase boundary [9, 10]. In particular, any straight segment of a RDS lamellar trajectory – or, equivalently, any locked lamellar plane – corresponds to a facet of the 2D Wulff form and thus to a deep minimum in the γ_B-plot.

During this study, apart from the initial eutectic-grain selection process, solidification runs were performed first by RDS, and then by DS. These two stages were separated by a short rest stage, during which the majority phase (δ) invaded the growth front. The space-time maps are therefore composed of two main parts: a lower part representing a π-RDS map; an upper part representing a conventional DS recording. An example is given in Section III A.

D. X-ray diffraction analysis

The orientation of the crystals in the **xyz** coordinate system was determined by X-ray diffraction analysis *in situ*, i.e. without removing the glass lids from the sample and without letting the sample cool below 60°. The pole figure method for texture analysis was used in order to get information on crystal mosaicity across the whole solidified area. To allow the use of conventional X-ray diffractometers, the upper glass lid was thinned with fluorhydric acid, before solidification, over an area covering the region of interest. X-ray measurements were performed in a Rigaku Smartlab 9kW diffractometer equipped with a home-made thermostatic chamber set at 60°. Sample transfer from the solidification bench to this thermostatic chamber were without any cooling of the region of interest below 60°. Constraints linked to the geometry of the samples prevented the detection of XRD peaks with an angle to the **y** axis (or polar angle) larger than about 63°, without negative consequences. The scanning pitch of the pole figures was of 1° for both the polar angle and the azimuth. The orientations of the different crystals present in a sample were calculated from the poles figure by standard methods. Details about the uncertainties resulting from the finite width of the XRD peaks are given in Section III A.

E. Identification of special interphase orientation relationships

A special interphase orientation relationship (OR) is defined by two mutually parallel low-index lattice planes – called coincident planes (CPs) – and two mutually parallel low-index lattice directions (CDs) belonging to the CPs. This set of CPs and CDs also defines an epitaxial interphase boundary, whose surface energy γ_{EB} characterizes the OR. As is common practice, we evaluated γ_{EB} using two criteria, namely, the atomic density and the misfit of the CPs. The misfit can be defined as the relative difference in atomic density of the CPs or, in a more refined way, as the deformation required to form a dense coincidence site lattice (CSL) along the interphase boundary [6]. It should be noted that low-energy heterophase boundaries with misfits as high as 15% were observed in epitaxial and eutectic growth [17, 18].

The atomic density of a lattice direction can be defined as the inverse of the shortest distance between neighbor atoms along this direction. The shortest vectors between neighbors are $\frac{1}{2} < 101 >^{\epsilon}$ and $\frac{1}{2} < 110 >^{\epsilon}$ in the ϵ phase, and $\frac{1}{2}[001]^{\delta}$, $\frac{1}{3}[210]^{\delta}$ and $\frac{1}{12} < 843 >^{\delta}$ in the δ phase. The atomic densities of these lattice directions are close to one another. The atomic density of a lattice plane can be defined as $\rho = n_{2D}d/\Omega$, where n_{2D} is the number of atoms per unit cell of the 2D lattice of the plane, d is the interplanar spacing and Ω is the volume of the 3D unit cell. For those lattice planes which contain several layers with different densities, the densest layer should be chosen. The densest lattice planes of ϵ are $\{111\}^{\epsilon}$ and those of δ are $\{2\bar{1}\bar{1}0\}^{\delta}$. For convenience, we shall express the atomic densities of the different lattice planes in units of the atomic density of $\{2\bar{1}\bar{1}0\}^{\delta}$ ($\rho_m \approx 9.57nm^{-2}$).

The method for the comparison of experimental data and theoretical ORs uses lists of equivalent lattice planes and directions of δ and ϵ sorted in decreasing order of atomic density (Table II). The method includes the following steps: (i) determination of the orientations of the crystals composing the EG under study; (ii) calculation of the misorientation angles between all the possible combinations of distinct δ and ϵ lattice planes in this EG; (iii) elimination of the combinations, for which the misorientation angle is larger than a predefined limit value (generally 2°); (iv) application of the same procedure to the lattice directions; (v) determination of a list of OR candidates combining the selected CP candidates with the CD candidates that belong to them; (vi) determination of the best OR candidate according to the misorientation angles of the CPs and CDs and the evaluation of γ_{EB}; (vii) characterization of the global orientation of the EG with respect to the sample by the angle ψ^{CP} between the CPs of the best OR candidate and the **yz** plane and the angle θ^{δ} between $(0001)^{\delta}$ and the **xz** plane. The misorientation angles of the CPs are denoted by Δ^{CP} and those of the CDs by Δ^{CD} hereafter.

δ phase	n_{2D}	ρ
$\{2\bar{1}\bar{1}0\}$	6	1
$\{0001\}$	2	0.799
$\{10\bar{1}0\}$	2	0.577
$\{2\bar{1}\bar{1}4\}$	6	0.514
$\{2\bar{1}\bar{1}2\}$	4	0.512
$\{30\bar{3}4\}$	6	0.416
$\{30\bar{3}2\}$	4	0.347
$\{10\bar{1}2\}$	2	0.328
ϵ phase	n_{2D}	ρ
$\{111\}$	4	1.059
$\{100\}$	2	0.947
$\{001\}$	2	0.865
$\{110\}$	2	0.670
$\{101\}$	2	0.639
$\{311\}$	4	0.566
$\{113\}$	4	0.530
$\{331\}$	4	0.432
$\{210\}$	2	0.424
$\{313\}$	4	0.415

TABLE II. First terms of the lists of equivalent lattice planes of the eutectic phases sorted in decreasing order of atomic density. ρ: atomic density in units of the atomic density of $\{2\bar{1}\bar{1}0\}^\delta$.

F. Nomenclature of special orientation relationships

We have built a nomenclature of the ORs of In-In_2Bi on the model of the nomenclature currently used for Al-Al_2Cu [5, 15, 16]. The following rules will apply:

(i) Sets of equivalent CPs are designated by capital letters, as in the following examples:

$$A = \{2\bar{1}\bar{1}0\}^\delta /\!/ \{111\}^\epsilon, \tag{1}$$

$$B = \{2\bar{1}\bar{1}0\}^\delta /\!/ \{100\}^\epsilon. \tag{2}$$

(ii) Sets of equivalent CDs are designated by numbers. Sets of equivalent ORs are thus denoted by dual symbols, as in the following examples:

$$A1 = \begin{cases} \{2\bar{1}\bar{1}0\}^\delta /\!/ \{111\}^\epsilon \\ [001]^\delta /\!/ < \bar{1}01 >^\epsilon \end{cases}, \tag{3}$$

$$A2 = \begin{cases} \{2\bar{1}\bar{1}0\}^\delta /\!/ \{111\}^\epsilon \\ [001]^\delta /\!/ < 1\bar{1}0 >^\epsilon \end{cases}. \tag{4}$$

(iii) Subscripts are used to distinguish between distinct ORs belonging to the same set of equivalent ORs. The following examples will be used below:

$$A1_1 = \begin{cases} (2\bar{1}\bar{1}0)^\delta /\!/ (111)^\epsilon \\ [001]^\delta /\!/ [01\bar{1}]^\epsilon ; \end{cases} \tag{5}$$

$$A1_2 = \begin{cases} (\bar{1}2\bar{1}0)^\delta /\!/ (\bar{1}11)^\epsilon \\ [001]^\delta /\!/ [01\bar{1}]^\epsilon ; \end{cases} \tag{6}$$

$$A3_1 = \begin{cases} \{2\bar{1}\bar{1}0\}^\delta /\!/ \{111\}^\epsilon \\ [483]^\delta /\!/ [10\bar{1}]^\epsilon . \end{cases} \tag{7}$$

A few additional points of terminology are:
(i) $A1_1$ has two variants related to each other by a π-rotation of the ϵ crystal around the axis normal to the CPs (π-variants).
(ii) One can switch from $A1$ and $A2$ trough a rotation by $\approx$58.5° of the ϵ crystal around the normal to the CPs ("in-plane" rotation). This remark can be generalized to any set of ORs sharing the same CPs.
(iii) Because of the similarity in local structure of the two phases, there exist sets of interrelated ORs at small angular distances from each other ("neighbor" ORs).

III. RESULTS

A. Grain structure of the samples

Figure 2 shows the space-time map of the solidification process undergone by Sample 1. This map reveals a fully locked growth dynamics, which will be studied in Section III D. Figure 3a shows the corresponding XRD pole figures. They reveal that Sample 1 contained a single δ crystal and two ϵ crystals (ϵ_1 and ϵ_2). In other words, it contained two eutectic grains, one (EG_1) formed by δ and ϵ_1 and the other (EG_2) by δ and ϵ_2. The boundary between EG_1 and EG_2 that is shown in Fig. 2 was traced in real time during solidification. The correspondence between EGs and XRD peaks was determined using X-ray-opaque masks. It is also apparent from Fig. 3 that the orientation of the crystals with respect to the sample is a singular one; however, this feature – as well as the presence of two EGs instead of one – is specific for Samples 1, 2 and 3, and will not be commented on until Section III E.

Figure 4 shows the substructures of two representative XRD peaks from Sample 1. These substructures contain a narrow high-intensity central peak and a broader low-intensity "base". The half widths of the two components are of about 1° and 2°, respectively. The same type of bimodal substructure was observed in all the samples studied. Five good-quality samples had the same peak and base widths as Sample 1. In the other four samples, described as medium quality herefater, the half width of

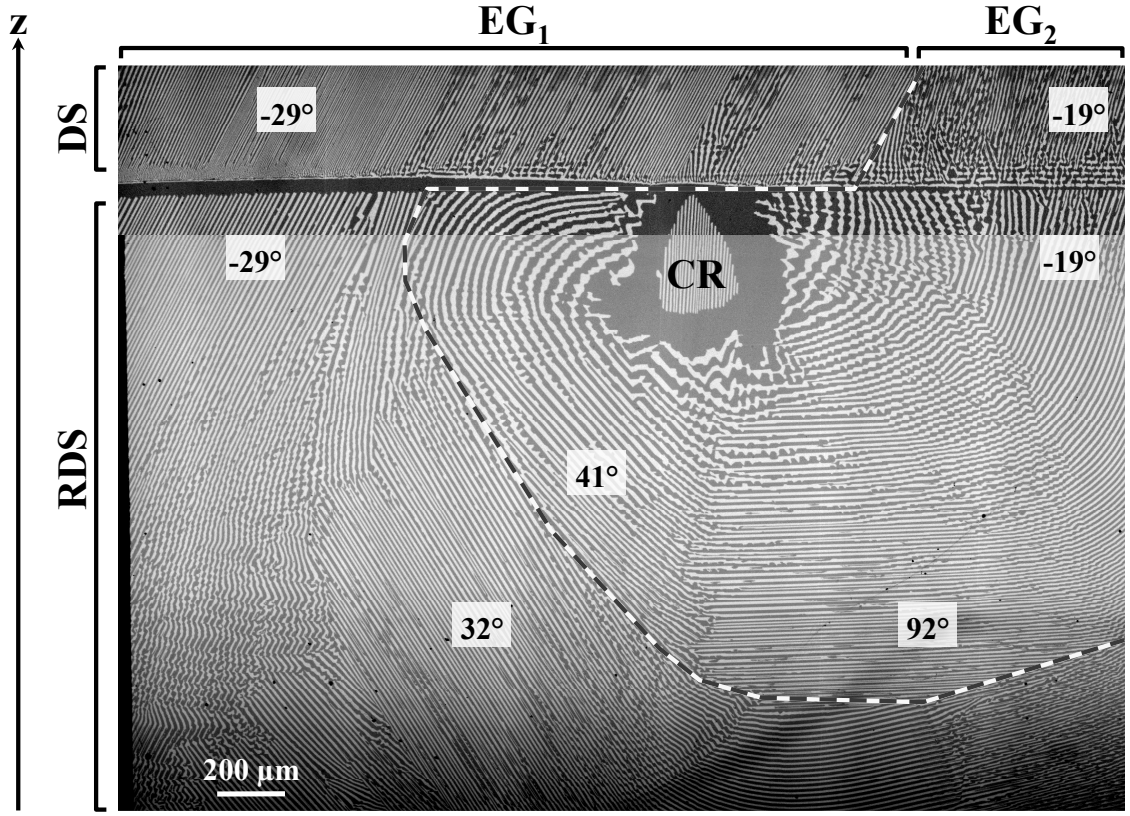

FIG. 2. Sample 1. Lower portion of the space-time map of the solidification process. The darker phase is δ (In_2Bi) and the lighter one is ϵ. The alloy is slightly hypereutectic. RDS: rotating directional solidification at 2.5×10^{-4} rad s^{-1}. DS: standard directional solidification at 0.5 μm s^{-1}. Only a portion of the total DS length (≈20mm) is represented. EG_1, EG_2: eutectic grains. Dash line: boundary between EG_1 and EG_2. Numbers: tilt angles of the lamellar trajectories with respect to **z** in various locked areas. CR: region near the center of rotation.

the central peak ranged from 1° to 3 ° and that of the base from 2° to 5 ° . Due to technical difficulties, a real-space investigation of the mosaic structure of the samples has not yet been possible. Preliminary investigations by EBSD performed *ex situ* at room temperature indicated that the width of the central peak probably reflects a crystal mosaicity of the bulk of the samples similar to that revealed by transmission electron microscopy studies in Al-Al_2Cu alloys [2], but did not cast much light on the origin of the broad bases of the peaks. We considered reasonable to use only the high-intensity central peaks in the crystal orientation calculations. The calculated margin of error on crystal orientations was approximately equal to the half width of the high-intensity peaks.

B. *A*-type orientation relationships

The main features of the five samples that exhibited a locked growth dynamics are displayed in Table III. It is striking that all the EGs of these samples had either $A1$ or $A2$ as best OR candidate. Let us explain this point in detail in the example of Sample 1 (Fig. 5). $A1_1$, as defined in Eq. (5), obviously was a good OR candidate for both the EGs of this sample, but the calculations yielded a large number of other potentially significant neighbor ORs. Those of them which belong to the $[001]^\delta // [101]^\epsilon$ zone are shown in Table IV. Incidentally, $A3_1$, as defined in Eq. (7), is only separated from

Sample	EG	OR	Δ^{CP} [deg]	Δ^{CD} [deg]	θ^δ [deg]	ψ^{CP} [deg]
1	1	$A1$	0.6	1.4	3.0	3
	2	$A1$	1.4	0.9	”	”
2	1	$A1$	0.5	2.0	8.0	7
	2	$A1$	0.3	1.8	”	”
3*	1	$A1$	1.0	4.8	25	3
	2	$A2$	3.6	3.5	”	30
4*	1	$A2$	2.1	2.7	27	27
5*	1	$A1$	2.6	3.3	41	36

TABLE III. Samples exhibiting a locked growth dynamics. Asterisk: medium-quality sample. EG: eutectic grain(s). OR: best OR candidate.

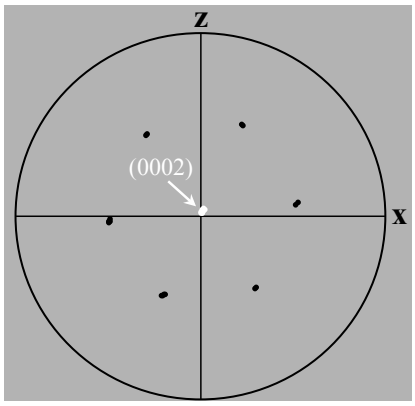

δ-phase
White: $(0002)^{\delta}$. Black: $\{2\bar{0}20\}^{\delta}$

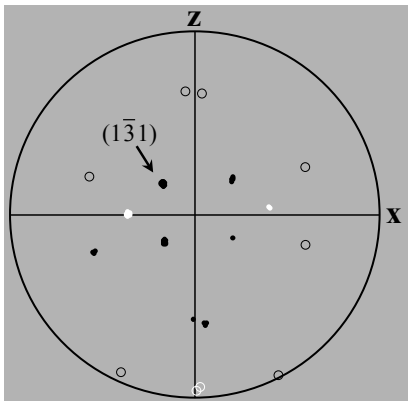

ε-phase
White: $\{200\}^{\varepsilon}$. Black: $\{311\}^{\varepsilon}$

FIG. 3. Sample 1. Pole figures. Open circles : location of non-detected peaks (polar angle > 63°).

$A1_1$ by an in-plane rotation of ≈0.3° and need not be distinguished from it. The data of Table IV are clearly in favor of $A1_1$. Moreover, Figure 6a shows that the

OR	CPs	ρ^{δ}	misfit	$\Delta_1^{\rm CP}$	$\Delta_2^{\rm CP}$
$D1_1$	$(\bar{1}010)^{\delta}/\!/(311)^{\epsilon}$	0.58	0.020	0.5	1.3
$A1_1$	$(2\bar{1}\bar{1}0)^{\delta}/\!/(111)^{\epsilon}$	1	0.057	0.6	1.4
$B1_1$	$(11\bar{2}0)^{\delta}/\!/(100)^{\epsilon}$	1	0.054	4.2	2.9
$C1_1$	$(\bar{1}100)^{\delta}/\!/(011)^{\epsilon}$	0.58	0.101	4.3	2.8
$D1_2$	$(01\bar{1}0)^{\delta}/\!/(\bar{3}11)^{\epsilon}$	0.58	0.020	8.0	6.5
$A1_2$	$(\bar{1}2\bar{1}0)^{\delta}/\!/(\bar{1}11)^{\epsilon}$	1	0.057	8.2	6.7

TABLE IV. Sample 1. Neighbor ORs belonging to the $[001]^{\delta}/\!/[101]^{\epsilon}$ zone. ρ^{δ}: atomic density of lattice planes of the δ phase. $\Delta_1^{\rm CP}$ and $\Delta_2^{\rm CP}$: misorientation angles of the CPs in EG_1 and EG_2, respectively.

2-D lattices of $(2\bar{1}\bar{1}0)^{\delta}$ and $(111)^{\epsilon}$ have similar pseudo-hexagonal motives, whose axes are approximately mutually parallel when their relative orientation is either

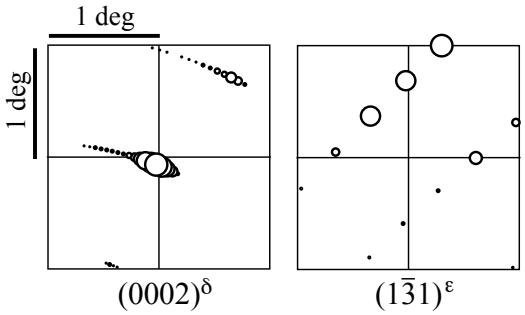

FIG. 4. Sample 1. Zoomed-in views of the XRD peaks marked by arrows in Fig 3. The sub-peaks are represented by circles of diameters proportional to their intensity.

$A1$ or $A2$. Coincident site lattices were obtained by superposing a deformed $(111)^{\epsilon}$ plane and an undeformed $(2\bar{1}\bar{1}0)^{\delta}$ plane. For $A1$ interface boundaries, a CSL with a coinciding-site density of about 1/2 (in ρ_m units) was obtained by means of a deformation of principal components $e_I \approx 0.073$ and $e_{II} \approx -0.018$ (Fig. 6b). For $A2$ interface boundaries, a CSL with a coinciding-site density of about 1/3 was obtained through a deformation of principal components $e_I \approx 0.006$ and $e_{II} \approx -0.055$ (Fig. 6c). Thus, $A1$ and $A2$ both have a low surface energy, according to generally accepted crystallographic criteria. They are jointly referred to as A-type ORs henceforth. The data of Table III can then be summed up as follows: all the locked EGs were A-type and all the A-type EGs were locked.

C. E-type orientation relationships

In all the samples that exhibited a floating growth dynamics, the best CP candidates were

$$E = \{1\bar{1}02\}^{\delta}/\!/\{111\}^{\epsilon}, \tag{8}$$

but the best CD candidates varied from sample to sample (Table V). In each sample, the selected E-type OR was part of a set of neighbor ORs. The selection was performed using the same criteria (misorientation angles, surface energy) as above. A representative example (Sample 9) is given in Fig. 8 and Table VI.

Sample	OR	$\Delta^{\rm CP}$ [deg]	CDs	$\Delta^{\rm CD}$ [deg]	θ^{δ} [deg]	$\psi^{\rm CP}$ [deg]
6	$E1$	0.5	$<021>^{\delta}/\!/<2\bar{3}1>^{\epsilon}$	5.0	5	59
7	$E2$	0.4	$<021>^{\delta}/\!/<\bar{2}\bar{1}3>^{\epsilon}$	0.2	20	55
8	$E1$	0.9	$<021>^{\delta}/\!/<2\bar{3}1>^{\epsilon}$	0.9	40	25
9*	$E3$	1.0	$<021>^{\delta}/\!/<0\bar{1}1>^{\epsilon}$	1.8	53	5

TABLE V. Samples exhibiting a floating growth dynamics. Asterisk: medium-quality sample. OR: best OR candidate.

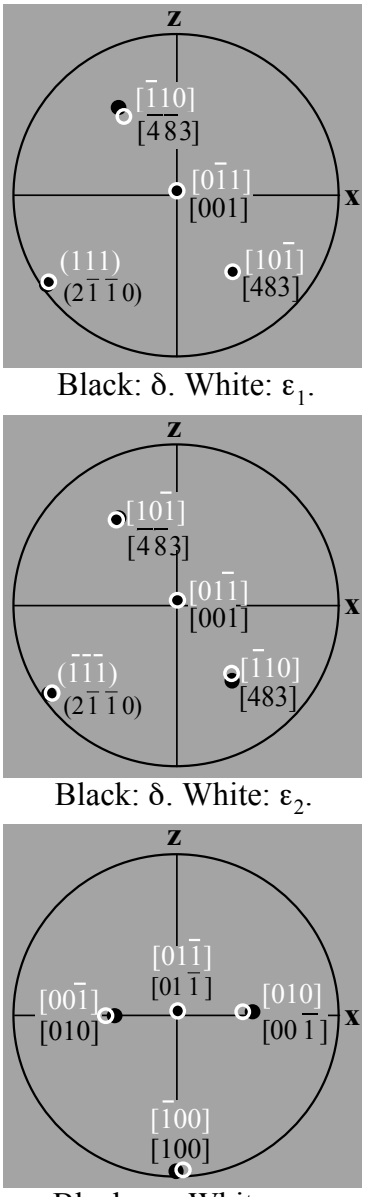

FIG. 5. Sample 1. Stereographic projections showing the existing orientation relationships between the δ and ϵ crystals in EG_1 (top) and EG_2 (middle), and between the two ϵ crystals (bottom).

OR	CPs	$\rho^\delta/\rho^\epsilon$ [deg]	Δ^{CP}	CDs [deg]	Δ^{CD}
$E3_1$	$(1\bar{1}02)^\delta /\!/ (111)^\epsilon$	0.31	1.0	$[\bar{2}01]^\delta /\!/ [0\bar{1}1]^\epsilon$	1.8
$F1_1$	$(10\bar{1}2)^\delta /\!/ (011)^\epsilon$	0.51	1.9	$[\bar{2}01]^\delta /\!/ [0\bar{1}1]^\epsilon$	1.8
	$(1\bar{2}10)^\delta /\!/ (31\bar{1})^\epsilon$	1.8	2.1	$[210]^\delta /\!/ [1\bar{3}0]^\epsilon$	3.5
	$(\bar{1}\bar{1}24)^\delta /\!/ (3\bar{1}3)^\epsilon$	1.2	3.6	$[\bar{1}10]^\delta /\!/ [\bar{2}\bar{3}1]^\epsilon$	5.4

TABLE VI. Sample 9. Main neighbor ORs. ρ^δ and ρ^ϵ: atomic densities of lattice planes in the δ and ϵ phases, respectively.

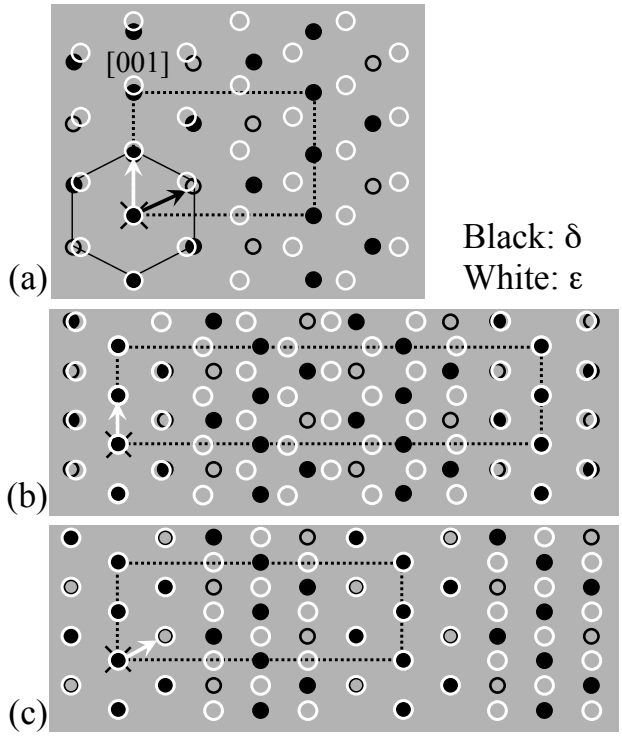

FIG. 6. 2-D lattices of $(2\bar{1}\bar{1}0)^\delta$ and $(111)^\epsilon$ superimposed. Cross: origin of coordinates. White arrow: $\frac{1}{2}[\bar{1}10]^\epsilon$. Black arrow: $\frac{1}{12}[483]^\delta$. Full *vs* open black circles : In *vs* Bi atoms. (a) $A2$ orientation relationship. Dotted line: unit cell of $(2\bar{1}\bar{1}0)^\delta$. (b) and (c) $A2$ and $A1$ orientation relationships with a slight deformation of the $(111)^\epsilon$ plane (see the text). Dotted lines: unit cell of the CSLs.

The relevance of E regarding the surface energy criterion is not immediately obvious since $\{1\bar{1}02\}^\delta$ has a low atomic density compared to $\{111\}^\epsilon$. However, the 2D lattice of $\{1\bar{1}02\}^\delta$ contains a pseudo-hexagonal motif very similar to the motif formed by the second-nearest neiborghs in $\{111\}^\epsilon$, in accordance with the fact that the density ratio of these planes is close to 1/3 (Fig. 7a). As shown in this figure, the $\{1\bar{1}02\}^\delta$ planes contain layers of composition InBi, which may contribute to lowering the energy of E-type interphase boundaries. In the example of Sample 9, a moderate ($e_I \approx 0.08$ and $e_{II} \approx -0.10$) deformation of the 2-D lattice of $(111)^\epsilon$ would suffice to produce a CSL including all the sites of the $(1\bar{1}02)^\delta$ plane for the $E3_1$ interphase boundary (Fig. 7b). Incidentally, this is also true of the $F1_1$ interphase boundary, since the density ratio of the CPs of this boundary is close to 1/2.

D. Locked lamellar planes

E-type samples showed quasi-circular or oval RDS lamellar trajectories, indicative of a near-isotropic or mildly anisotropic floating growth dynamics [8]. By con-

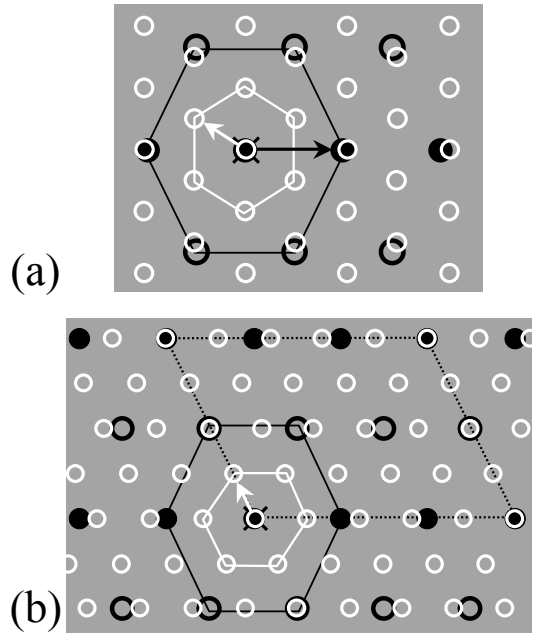

FIG. 7. 2-D lattices of $(1\bar{1}02)^{\delta}$ and $(111)^{\epsilon}$ superimposed. Cross: origin of coordinates. White arrow: $\frac{1}{2}[101]^{\epsilon}$. Black arrow: $[110]^{\delta}$. Full *vs* open black circles : In *vs* Bi atoms. (a) Symmetrical orientation relationship (not observed). (b) $E3$ orientation relationship with a slight deformation of the $(111)^{\epsilon}$ plane (see the text). Dotted line: unit cells of the CSL.

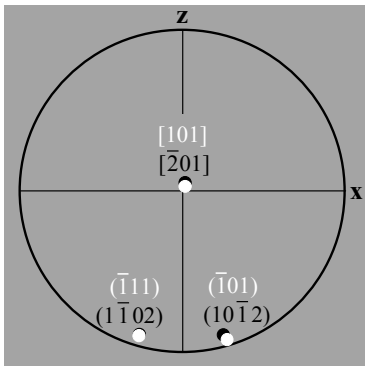

FIG. 8. Sample 9. Stereographic projection showing the coincident lattice planes and directions of $E3_1$ and $F1_1$ (see Table VI).

trast, *A*-type samples displayed polygonal-shaped RDS lamellar trajectories characteristic of a strongly locked growth dynamics (Fig. 2). Each rectilinear segment of an RDS trajectory is the intersection of a particular locked lamellar plane (LP) and the sample plane. Knowing that LPs may not be perpendicular to the sample plane [8], we characterized their orientation by two angles, namely, the tilt angles with respect to **z** of their trace on the **xz** plane (longitudinal tilt angles) and the **yz** plane (transverse tilt angles). Longitudinal tilt angles were measured in space-time maps with a margin of error of $\pm 1^{o}$. Transverse tilt angles were measured in metallographic transverse cross-sections in some samples and were found to be smaller than the experimental uncertainty ($\approx 5^{o}$), except in Sample 5. Longitudinal tilt angles will be simply called tilt angles henceforth.

As shown in Fig. 9, each of the two EGs of Sample 1 contained three different LPs called LP_1, LP_2 and LP_3, which lay a few degrees from $(2\bar{1}\bar{1}0)^{\delta}$, $(11\bar{2}0)^{\delta}$ and $(\bar{1}2\bar{1}0)^{\delta}$ – and thus from the CPs of $A1_1$, $B1_1$ and $A1_2$, respectively (see Table IV). The angle between LP_1 and $(2\bar{1}\bar{1}0)^{\delta}$ was of about 3^{o} in EG_1 and 6^{o} in EG_2. In each EG, let us take the trace of $(2\bar{1}\bar{1}0)^{\delta}$ instead of **z** as origin of the tilt angles. As shown in Figure 10, the tilt angles thus measured were close to 0^{o} (LP_1), 60^{o} (LP_2) or 120^{o} (LP_3) in Samples 1 to 4. In Sample 5, the following facts were found: only two locked planes (LP_2 and LP_3) were observed; these planes had large transverse tilt angles and lay close to the $[120]^{\delta}$ and $[1\bar{1}0]^{\delta}$ zones, respectively; the floating lamellae observed in the vicinity of 0^{o} also had a relatively large transverse tilt angle (Fig. 11a). Given that all the *A*-type EGs had the same γ_B-plot except that the global orientation of it changed from EG to EG, the above observations suggest that the γ_B-plot of *A*-type EGs contains three deep valleys, which intersect the $(0001)^{\delta}$ plane a few degrees from the $\{2\bar{1}\bar{1}0\}^{\delta}$ poles and change from deep to shallow at some distance from this plane (Fig. 11b).

E. Twin ϵ crystals and the ϵ-(In) transition in *A*-type samples

Let us consider the orientation relationships between the two ϵ crystals of the two-grained samples, and between these crystals and the coordinate system of the sample. Within experimental error, the main findings are the following:

(i) The two ϵ crystals of Sample 1 were twin crystals related to each other by a π-rotation about a $< 011 >^{\epsilon}$ axis, which was nearly perpendicular to the sample plane (Fig. 5b). The ORs of the two EGs were thus π-variants of $A1_1$;

(ii) Sample 2 had the same two-grained structure as Sample 1 with only a slightly different orientation of the δ crystal with respect to the sample plane (Table IV).

(iii) In Sample 3, EG_1 had a $A1$ OR on a $\{2\bar{1}\bar{1}0\}^{\delta}$ plane; EG_2 had a $A2$ OR on another $\{2\bar{1}\bar{1}0\}^{\delta}$ plane; ϵ_1 and ϵ_2 were twin crystals related to each other by a π-rotation about a $< 211 >$ axis (Fig. 12). The twin axis was nearly perpendicular to the sample plane.

These observations strongly suggest that *A*-type ORs were created in the nucleation stage by epitaxial nucleation of one phase onto the other. Since, after their formation by nucleation, the crystals were cooled to room temperature and then reheated up to the eutectic temperature, a preliminary requirement for this assumption

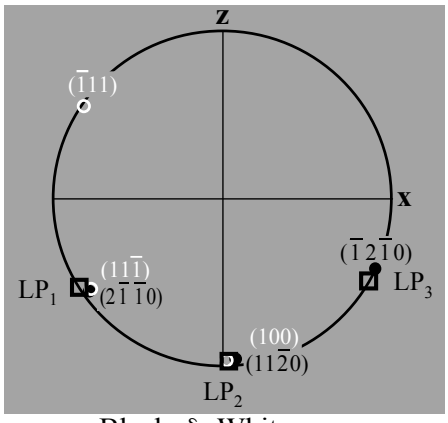

Black: δ. White: ε_1.

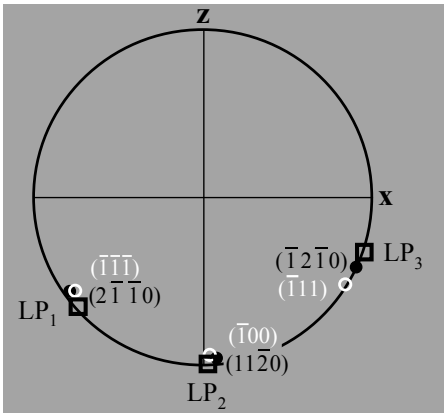

Black: δ. White: ε_2.

FIG. 9. Sample 1. Stereographic projections showing the coincident lattice planes of $A1_1$, $B1_1$ and $A1_2$ (see Table IV) in in EG_1 (top) and EG_2 (bottom). LP_1, LP_2 and LP_3: locked lamellar planes.

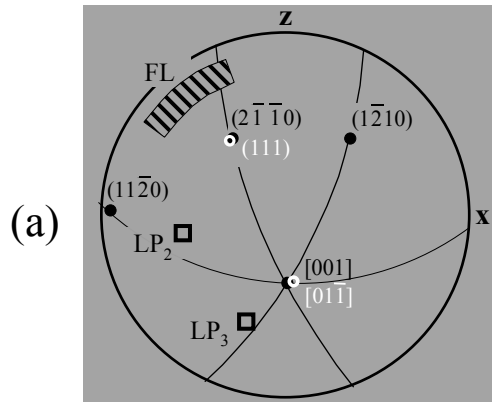

Black: δ. White: ε.

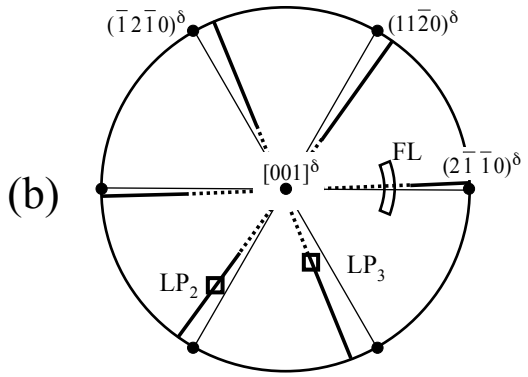

FIG. 11. Stereographic projections. (a) Sample 5. Coincident lattice planes and directions, and locked lamellar planes (LP_1 and LP_2). FL: floating lamellar planes. (b) Sketch of the valleys of the γ_B-plot of $A1$ EGs in the coordinate system of the δ phase. Continuous lines: deep valleys. Dotted lines: shallow valleys.

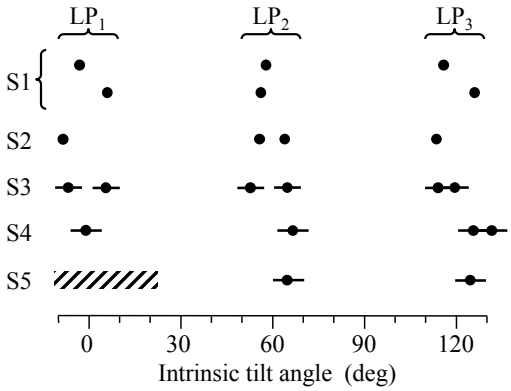

FIG. 10. Tilt angles of locked lamellar planes (LPs) referred to the trace of $(2\bar{1}\bar{1}0)^\delta$ in Samples 1 to 5. For technical reasons, it was not possible to separate data from the different EGs in Samples 2 and 3, as was done in Sample 1. Hatched area: floating lamellar planes. Thick lines: margins of error.

to be justified is that the orientation of the crystals was preserved through the eutectoid transformation at 49°. To investigate this matter, we cycled some directionally solidified samples between 60° and 30° in the RX diffractometer and collected XRD pole figures at these temperatures. The results obtained with Sample 2 are shown in Figure 13. It can be seen that the ϵ-(In) transition consisted of a deformation of the unit cell through which the 4-fold axis of the ϵ phase transformed into a 2-fold axis of the (In) phase and vice versa, while the orientation of the axes was approximately preserved. As there are two 2-fold axes and a single 4-fold axis per crystal, one ϵ crystal might give rise, upon cooling, to two (In) variants, which in turn might give rise to three ϵ variants upon reheating. This was not observed in A-type samples. In fact, no changes at all were observed in the pole figures of the phases between the beginning and end of a thermal cycle, even at the sub-structure level (Fig. 13c). The orientation and substructure of the (single) δ crystal contained in A-type samples were also perfectly preserved during the eutectoid transition.

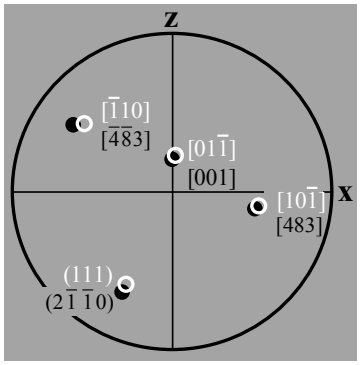

Black: δ. White: ε_1.

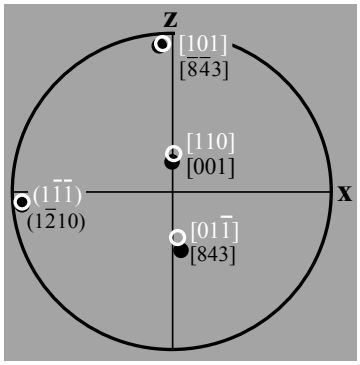

Black: δ. White: ε_2.

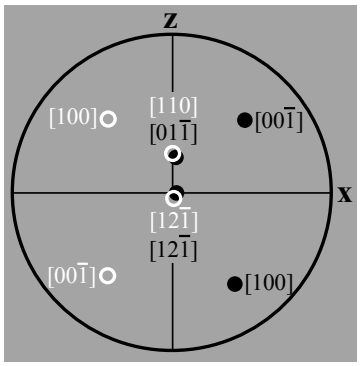

Black: ε_1. White: ε_2.

FIG. 12. Sample 3. Stereographic projections showing the existing orientation relationships between the δ and ϵ crystals in EG_1 (top) and EG_2 (middle), and between the two ϵ crystals (bottom).

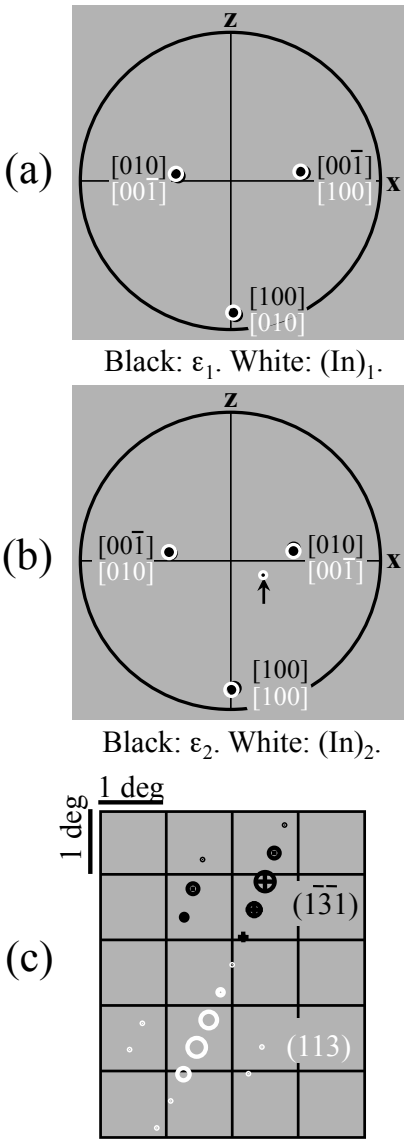

FIG. 13. Sample 2. (a) and (b) Stereographic projections of mutually transforming ϵ and (In) crystals in the two EGs (see the text). (c) Zoomed-in view of the XRD peaks marked by an arrow in (b). Black circles: ϵ before thermal cycling. Black crosses : ϵ after thermal cycling. White circles: (In) at 30°.

IV. DISCUSSION

This study has clearly demonstrated a strong correlation between special interphase orientation relationship and locked lamellar growth, in agreement with theoretical predictions. However, it has also revealed several unexpected facts, which need to be discussed. A first point is the relatively large (3 to 6°) angular deviation found between the locked lamellar plane LP_1 and the CPs in *A*-type EGs. According to recent theoretical and numerical studies, the normal to a locked lamellar plane points is unlikely to lie at more than 1° from the direction of a minimum of the γ_B-plot [9, 10]. It must therefore be admitted that the minimum of the γ_B-plot corresponding to LP_1 lies several degrees from the normal to the CPs in *A*-type EGs. In fact, a similar assumption about the other two locked lamellar planes of *A*-type EGs has been made above: LP_3, for example, was assumed to lie somewhere between a $(\bar{1}2\bar{1}0)^\delta$ and a $(\bar{1}11)^\epsilon$ plane making an angle of about 8° with each other. Speculations on the structure of these interphase boundaries on the atomic scale would be useless. We can simply note that the CPs of *A*-type EGs are not parallel to a plane of symmetry of the γ_B-plot and that, therefore, there is no

obvious reason for them to coincide with a minimum of the γ_B-plot.

Another interesting question raised by our findings is the formation mechanism of A-type ORs. We first note that the small (1 to 3°) orientation scatter found in these samples discards any hypothesis based on a slow rearrangement of the crystal orientations during growth [3]. In our case, the best assumption seems to be that A-type ORs were created in the nucleation stage and preserved without substantial change during the ensuing growth process. As shown above, this would be compatible with the ϵ-(In) transitions undergone by the crystals before the onset of directional solidification. Concerning the nucleation process itself, two scenarios are admissible, given the experimental uncertainties: either δ nucleated first from the liquid and the two ϵ crystals nucleated simultaneously on the same (in Sample 1 and 2) or different (in Sample 3) $\{2\bar{1}\bar{1}0\}$ planes of the δ nucleus, or ϵ nucleated first in the form of a twin crystal. In any case, an interaction between the nucleus and the sample walls must have taken place since the twin axis of the ϵ crystal were found to be nearly perpendicular to the sample plane.

V. CONCLUSION

Two different types of special interphase orientation relationships, namely,

$$A = \{2\bar{1}\bar{1}0\}^{\delta} /\!/ \{111\}^{\epsilon} \tag{9}$$

and

$$E = \{1\bar{1}02\}^{\delta} /\!/ \{111\}^{\epsilon}, \tag{10}$$

have been identified in thin In-In_2Bi samples. All the A-type eutectic grains exhibited a strongly locked lamellar growth, while all the E-type ones displayed a more or less anisotropic floating lamellar growth. As shown above, the surface energy of A-type interphase boundaries is substantially smaller than that of E-type ones, according to well-established crystallographic criteria. Thus the results of this study unequivocally validate the assumption of a link between locked lamellar growth and epitaxial interphase boundaries that underlies current theories of anisotropy effects in lamellar eutectic growth [9, 10]. As a final remark, we wish to stress that the good agreement between experimental and theoretical results is at present limited to 2-D lamellar eutectics. This study has indeed shown that even a thin lamellar eutectics can cease to be a 2-D system under the influence of a strong anisotropy of the surface energy of the interphase boundary. Future studies should therefore focus on anisotropy effects related to interphase boundaries in bulk lamellar eutectics.

Acknowledgments

We thank Richard Soucek for his ongoing technical help. We are greatly indebted to Gwenaëlle Rousse for her help in performing and analyzing X-ray powder diffraction patterns and Sarah Hidki for performing the X-ray pole figure measurements. We warmly thank Ulrike Hecht for many enlightening discussions and for performing EBSD measurements. This work was financially supported by ANPHASES M-ERA.NET project (ANR-14-MERA-004).

[1] Hogan LM, Kraft RW, Lemkey FD. Adv. Mater. Res. 1971;5:8.
[2] Davies IG, Hellawell A. Phil Mag 1969;19: 1285.
[3] Davies IG, Hellawell A. Phil Mag 1970;20: 1255.
[4] Cantor B, Chadwick GA. J Cryst Growth 1974;23: 12.
[5] Hecht U, Witusiewicz VT, Drevermann A, Rex S. Trans. Indian Inst. Met. 2005;58:545
[6] Sutton A.P., Balluffi R.W. Interfaces in Crystalline Materials; P332 Oxford University Press; 2009.
[7] Akamatsu S, Bottin-Rousseau S, Faivre G. Acta Mater 2011;59: 7586.
[8] Akamatsu S, Bottin-Rousseau S, Şerefoğlu M, Faivre G. Acta Mater 2012;60: 3206.
[9] Akamatsu S, Bottin-Rousseau S, Şerefoğlu M, Faivre G. Acta Mater 2012;60: 3199.
[10] Ghosh S, Choudhury A, Plapp M, Bottin-Rousseau S, Faivre G, Akamatsu S. Phys Rev E 2015;91: 022407.
[11] Massalsky TB, Subramanian PR, Okamoto H, Kasprzak L. Binary Alloys Phase Diagram, 2nd Ed. Materials Park, ASM Inst.
[12] Becker JH, Chalmers B, Garrow EG. Acta Cryst 1952;5: 853.
[13] Remaut G, Lagasse A, Amelinckx S. Phys. Stat. Sol. 1964;6: 723.
[14] Akamatsu S, Moulinet S, Faivre G. Metall Mater Trans A 2001;32:2039.
[15] Bonnet R, Durand F. Conference on in situ Composites; P209. Public NMAB 308-I, Lakerville, USA; 1973.
[16] Kokotin R, Hecht U. J. Eur. Ceram. Soc. 2014;86:30-37.
[17] Merkle KL, Buckett MI, Gao Y. Acta Met Mater 1992;40:S249-S257.
[18] Ohashi Y, Yasui N, Suzuki T, Watanabe M, Den T, Kamada K, Yokota Y, Yoshikawa A. Comput. Mater. Sci. 2014;34:3849-3857.